Reduction of streak artifacts caused by low photon counts utilizing an image-based forward projection in computed tomography

doi: https://doi.org/10.1016/j.compbiomed.2021.104583

Computers in Biology and Medicine 135 (2021) 104583

Contents lists available at ScienceDirect

Computers in Biology and Medicine

journal homepage: www.elsevier.com/locate/compbiomed

Reduction of streak artifacts caused by low photon counts utilizing an image-based forward projection in computed tomography

Shinji Niwa [a,b], Katsuhiro Ichikawa [c,*], Hiroki Kawashima [c], Tadanori Takata [d], Shuhei Minami [d], Wataru Mitsui [d]

[a] Department of Medical Technology, Nakatsugawa Municipal General Hospital, 1522-1 Komanba, Nakatsugawa, Gifu, 508-0011, Japan
[b] Division of Health Sciences, Graduate School of Medical Science, Kanazawa University, 5-11-80 Kodatsuno, Kanazawa, 920-0942, Japan
[c] Institute of Medical, Pharmaceutical and Health Sciences, Kanazawa University, 5-11-80 Kodatsuno, Kanazawa, Ishikawa, 920-0942, Japan
[d] Radiology Division, Kanazawa University Hospital, 13-1 Takara-machi, Kanazawa, 920-8641, Japan

ARTICLE INFO

Keywords:
Computed tomography
Streak artifact
Radiation dose
Sinogram
Spatial resolution

ABSTRACT

Background: The streak artifacts in computed tomography (CT) images caused by low photon counts are known to be effectively suppressed by raw-data-based techniques. This study aims to propose a technique to reduce the streak artifact without accessing the raw data.

Methods: The proposed streak artifact reduction (SAR) technique consists of three steps: numerical forward projection to a CT image, adaptive filtering of the generated sinogram, and image reconstruction from the processed sinogram. The authors have expanded the two-dimensional method (2D-SAR) to three dimensions (3D-SAR) by using consecutive CT images. The modulation transfer function (MTF), the image noise (standard deviation), and the visibility of comb-shaped objects were evaluated at a low dose of 5 mGy. Using anthropomorphic abdominal and chest phantoms, CT images and the artifact index (AI) were compared between 3D-SAR and two types of iterative reconstruction (IR).

Results: Sufficient artifact reductions associated with 54% and 61% reduction of noise for 2D- and 3D-SAR, respectively, were obtained in the phantom images, although the 50%MTF decreased by 28%. The visibility of the combs was improved with both the 2D- and 3D-SAR methods. The AI results of 3D-SAR were better than one type of IR and almost equal to the other type of IR, which was consistent with observed artifacts.

Conclusion: Both 2D-SAR and 3D-SAR have turned out to be effective in reducing streak artifacts. The proposed technique will be an effective tool since it needs no raw data, and thus can be applied to any CT images produced by a wide variety of CT systems.

1. Introduction

The streak artifact due to low photon counts tends to occur in computed tomography images obtained with low radiation doses [1]. Since the human body is oblong in shape, streak artifacts tend to run horizontally in body CT images. Further, additional streak artifacts are introduced by the photon noise resulting from the additional attenuation caused by the bone structure. For clinical diagnosis, these artifacts are a nuisance to radiologists because they can obstruct the view of the underlying anatomy and render the CT images unsuitable. Thus, several raw-data-based techniques have been proposed to reduce the streak artifacts caused by low photon counts (hereinafter simply referred to as "streak artifact(s)"), including those which smooth excessive photon noise caused by a highly attenuated x-ray adaptively according to the noise level [2–4]. It is generally difficult to reduce streak artifacts by means of image-based processing, which cannot make use of the measured attenuation values and the photon statistics [4]. The directions, locations, and quantity of streak artifacts cannot be clearly identified without attenuation data in the raw-data. Thus, the raw-data-based techniques that reduced the origins of streak artifacts, such as the one mentioned above, have also been proposed. Whereas iterative reconstruction (IR) techniques are clinically available, only the full versions of IR techniques that perform multiple iterations between the raw-data space and the image space incorporating sophisticated

* Corresponding author.
E-mail addresses: shinji-niwa.gifu@aria.ocn.ne.jp (S. Niwa), ichikawa@mhs.mp.kanazawa-u.ac.jp (K. Ichikawa), kawa3@med.kanazawa-u.ac.jp (H. Kawashima), t-takata@med.kanazawa-u.ac.jp (T. Takata), s_minami@med.kanazawa-u.ac.jp (S. Minami), w_mitsui@med.kanazawa-u.ac.jp (W. Mitsui).

https://doi.org/10.1016/j.compbiomed.2021.104583
Received 2 April 2021; Received in revised form 2 June 2021; Accepted 11 June 2021
Available online 26 June 2021

system models are effective in reducing streak artifacts [5–7]. The hybrid-type IR techniques that reduce the image noise mostly in the image space to keep the reconstruction time as short as with the conventional filtered back projection (FBP) can smooth streak artifacts but cannot reduce them [8]. More recently, deep-learning-based reconstruction (DLR) has been clinically available. DLR separates noise from signals by applying backpropagation to reconstruction processes based on differences between the ground truth images and low dose images, and suppresses the image noise without impacting anatomical structures (signals) [9]. DLR appears to be effective in streak artifact reduction as far as observed in images in recent reports [10,11]. However, it requires a very sophisticated reconstruction device; thus, its use is still limited to high-end CT systems incorporating expensive options for DLR. Meanwhile, the full version of IR, which also requires an additional device for reconstruction, takes as long as 10–30 min (primarily for reconstruction) to complete one scan, which renders it unsuitable for routine use [12,13].

Consequently, the streak artifacts still remain visible in many of clinical images, and it is almost impossible to restore the clean image because one cannot access and modify the reconstruction program inside the CT system for reducing streak artifacts. Moreover, as for CT images transferred from a remote location, there is no way of accessing the corresponding raw-data in the first place.

The image-based forward projection techniques can be used for a CT image to obtain projection data that mimic the real raw-data corresponding to the image. Particularly, with the full versions of IR, the projection data generated by image-based forward projection is necessary in a process that compares it with the real raw data to estimate the compensation data for reducing image noise and/or artifacts [14]. Also, forward projection has been used in studies to insert simulated lesions into patient images, reproducing realistic lesion appearances [15] and to reduce metal artifacts [16]. These processes require precise geometric information for the corresponding acquisitions to correctly perform forward projection. Thus, forward projection is effective only in each dedicated development (study) environment that can communicate with CT developers. In theory, image data can be reproduced (reconstructed) from the projection data generated using an image-based forward projection based on any geometric assumption, via the corresponding inverse (back projection) process. Therefore, data processing using such projection data is expected to be effective in improving CT image quality. However, to the best of our knowledge, there have been no reports to date that investigate the usefulness of image-based forward projection, other than IR, lesion insertion, and metal artifact reduction. Since a CT image represents a distribution of the attenuation coefficient within a slice, image-based forward projection produces attenuation data nearly proportional to the real attenuations at each projection angle. Thus, the noise levels in the data can be approximated from these attenuation data using the presumed radiation dose input. Therefore, we expect that the projection data would be useful in reducing streak artifacts just as with conventional raw-data-based processing and that the streak artifacts that still remain in existing CT images can be reduced without accessing the raw data.

This study aims to propose a technique to reduce streak artifacts by working on the projection data generated by image-based forward projection and to evaluate its performance of artifact reduction through physical image quality measurements and image comparisons with two hybrid types of IR routinely used in clinical CT examinations.

2. Methods and materials

2.1. Basic procedures

In our proposed streak artifact reduction (SAR) processing, first, a virtual sinogram (projection data set) was generated by a numerical parallel-beam forward projection performed in an angle range of $0° \leq \theta < 180°$. Then, the generated sinogram was adaptively processed using a weighted summation between this generated sinogram and its smoothed version. Basically, the portions having higher attenuations were weighted higher by the smoothed sinogram. Finally, a CT image was reconstructed from the processed sinogram.

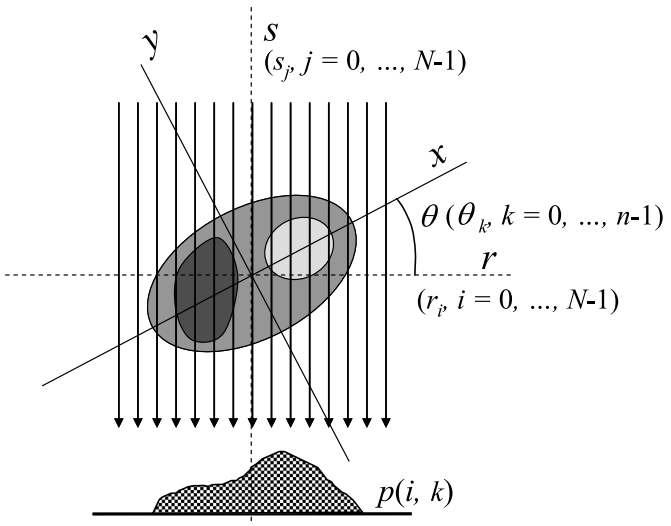

Fig. 1. Coordinate relationship in numerical parallel forward projection to generate virtual projection data. For each discrete angle θ_k ($k = 0, \ldots, n$-1), along a ray projection at a discrete position r_i ($i = 0, \ldots, N$-1), sampled data at s_j ($j = 0, \ldots, N$-1) were accumulated to $p(i, k)$. Bicubic interpolation was used for the sampling.

2.2. Application

The application of the proposed technique is limited to the body CT images spanning from the chest to the pelvis that are reconstructed with the appropriate display fields of view (DFOVs) covering the full body contour, where the correct projection data is estimated by image-based forward projection. Moreover, CT images that include severe metal artifacts or data corruption due to aliasing errors cannot be used because the projection data cannot be correctly estimated.

2.3. Forward projection

Prior to forward projection, each pixel value in the CT number data $c(n, m)$, a matrix of 512 by 512, was converted to $c_{att}(n, m)$ by adding 1000 to it. As a result, each item of data in $c_{att}(n, m)$ was made proportional to its attenuation coefficient, based on the commonly-used equation for calculating CT numbers from attenuation data.

Fig. 1 shows the relationship between the coordinates in numerical parallel-beam forward projection and those in the rotated c_{att} data. As shown in this figure, we employed a rotation-based method in which a projection data array remains fixed and the image is rotated through interpolation [17]. In each ray position at r_i ($i = 0, \ldots, N$-1), the data sampling at s_j ($j = 0, \ldots, N$-1) was repeated and accumulated to $p(i, k)$ at each projection angle θ_k ($k = 0, \ldots, n$-1) as follows:

$$p(i,k) = \sum_{j=0}^{N-1} c'_{att}(x(i,j), y(i,j)) \tag{1}$$

$$x(i,j) = r_i \cos(\theta_k) - s_j \sin(\theta_k), \tag{2}$$

$$y(i,j) = r_i \sin(\theta_k) + s_j \cos(\theta_k), \tag{3}$$

where x and y are x- and y-positions in the rotated image coordinate system, respectively, and $c'_{att}(x, y)$ is the data sampled in c_{att}. Bicubic interpolation was used for the sampling with an α parameter of -0.5 because this method can produce a smaller spatial resolution loss

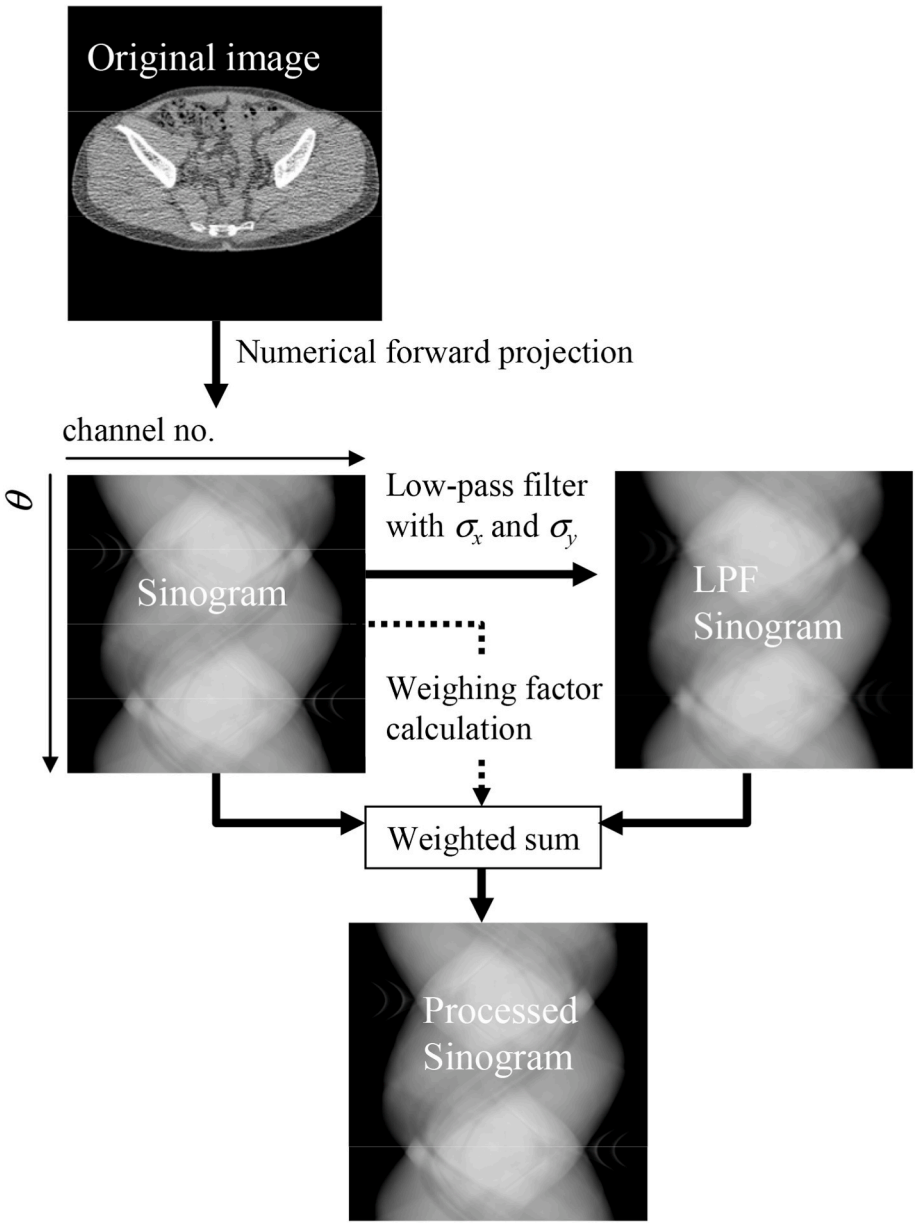

Fig. 2. Outline of adaptive sinogram filtering. The sinogram generated through numerical forward projection was processed by a 2-dimensional (2D) Gaussian filter with a parameter combination of σ_x and σ_y. A weighted summation was performed based on the attenuation values in the sinogram, which yielded a processed sinogram, where areas with higher attenuations were more smoothed.

compared with the bilinear technique [18]. The sampling interval was set at half the pixel pitch of the CT image; thus 1024 points were required ($N = 1024$) for each of the r_i and s_j positions. A total of 800 projections ($n = 800$) were made at intervals of $180°/n$ within $0° \leq \theta < 180°$. Through this process, a set of sinogram data in a 1024×800 matrix was obtained. Although we could have further increased the projection number, we settled for this value based on the results of a preliminary investigation that compared original images and their corresponding reconstructed images.

In this numerical projection, we did not employ the fan-beam geometry. The information in CT image files alone turned out to be insufficient to determine the fan-beam geometry that is precisely identical to that of CT system we used. When we preliminarily tested fan-beam forward projections with several geometric assumptions, we did not see any advantages in the reduction of artifacts compared with the parallel method we adopted in this study.

2.4. Adaptive sinogram filtering

Fig. 2 illustrates the outline of adaptive sinogram filtering in SAR. A smoothed version of the sinogram was produced by using a two-dimensional (2D) Gaussian filter with standard deviation parameters σ_x and σ_y. While both σ_x and σ_y contribute to noise filtering, σ_y should be carefully increased because a larger σ_y may reduce the detector's temporal resolution, causing non-negligible artifacts.

The peak values [$v(k)$, $k = 0, \ldots, n\text{-}1$] in respective projection data (i.e., each horizontal profile in the sinogram) were identified; then, the maximum and minimum peak values, v_{max} and v_{min}, were determined. To effectuate adaptive sinogram filtering, a weighted summation between the original sinogram and the smoothed sinogram was performed by using weighting factors $w(i, k)$ as follows:

$$w(i, k) = (p(i, k) - (v_{min} \times R)) / (v_{max} - v_{\min} \times R), \quad (4)$$

where R denotes an adjustment coefficient for v_{min}. While lower R values

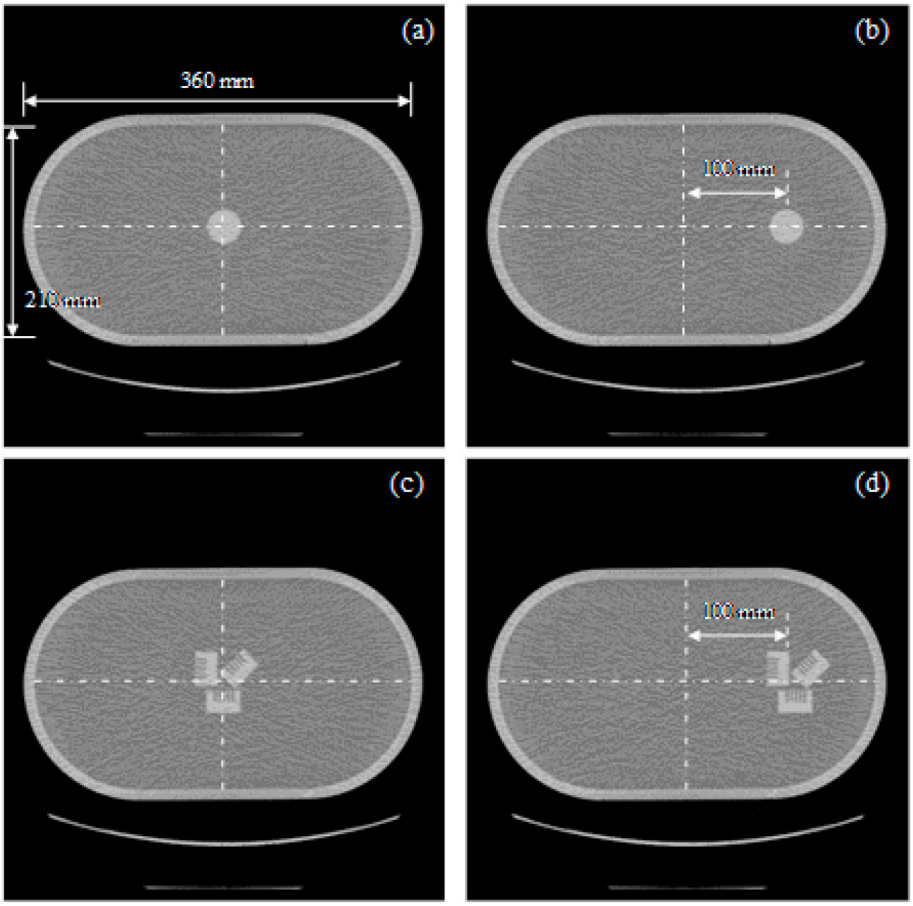

Fig. 3. Image examples of an elliptic cylindrical water phantom in which a rod object (rod phantom) (a, b) or an assembly of three identical comb-shaped objects (bar-pattern phantom) with horizontal, vertical, and 45° alignments (c, d) was placed. The rod phantom and the bar-pattern phantom were employed to measure the modulation transfer function (MTF) and to visually assess the clarity of the bar pattern (bar-pattern visibility), respectively.

contribute more to the reduction of streak artifacts, they tend to lower the spatial resolution. In this study, a fixed R value of 0.9 was used throughout the investigations to suppress the degradation of spatial resolution. The relationship between the data level (attenuation) and its variation (standard deviation) in a sinogram is known to be nonlinear (e.g., exponential) [3]. However, we found that the linear calculation of Eq. (4) for determining the weighting factors was effective enough in reducing streak artifacts in preliminary investigations. While the noise reduction effect of Gaussian filtering is rather small at low data levels, it increases as the data level increases, limiting the nonlinearity. The noise that causes streak artifacts tends to have more high-frequency components easily reduced by noise filtering. Instead of the Gaussian filter mentioned above, we preliminarily tested a median filter and a bilateral filter as edge-preserving noise reduction techniques, but found them unusable: They produced new artifacts around bone edges presumably due to inconsistencies in projection data resulting from the non-linear filtering processes in them. The adaptive filtering method using the weighted sum was selected because the processing time was reasonably short and the performance was sufficient for this pilot study that examines the feasibility of the streak artifact reduction achievable without using the raw-data.

Currently, tube current modulation (TCM), which controls the tube current adaptively according to the patient's body size is commonly used in clinical CT examinations. Thus, the proposed technique is intended to be used under the regulated noise condition according to each setting of TCM. Owing to this limited application, σ_x and σ_y can be determined also according to the setting of TCM by observing the reduction level of the streak artifact.

2.5. Filtered back projection

Prior to the filtering process in filtered back projection (FBP), the horizontal data number of the sinogram was increased to 2048 by padding zeros to both its left side and right side to enable the filtering process. For each horizontal profile in the sinogram, a one-dimensional (1D) fast Fourier transform (1D-FFT) was applied; then, the derived Fourier coefficients were multiplied by Shepp-Logan type filter function data. Finally, a filtered profile was obtained by applying an inverse 1D-FFT.

For each pixel location with $x'(n, m)$ and $y'(n, m)$ in an image to be reconstructed, the r position $r_{n,m}$ in the filtered sinogram at θ_k can be calculated as follows:

$$r_{n,m} = x'(n,m)\cos(\theta_k) + y'(n,m)\sin(\theta_k). \quad (5)$$

The sampling data at $r_{n,\ m}$ was obtained through one-dimensional cubic interpolation with an α parameter of -0.5; then the sampled data was integrated (back-projected) to the pixel. By repeating this process for all the projection angles, the image was successfully reconstructed from the processed sinogram. Finally, a constant value of 1000 was subtracted from all the pixel data to recover their CT numbers (This is to compensate for the addition of 1000 performed prior to the forward projection).

2.6. Three-dimensional processing

The above-mentioned 2D processing of SAR (2D-SAR) can be extended to three-dimensional (3D) processing (3D-SAR) using a CT

image stack (consecutive CT images), which is required to have a thin slice thickness of 1.0 mm or less. First, a z-directional Gaussian filter (with parameter σ_z) was applied to the image stack. The remainder of the process is two-dimensional. The numerical forward projection was performed for both the original data c_{att} and the z-smoothed data cs_{att} to generate two sinograms; then, a 2D Gaussian filter with σ_x and σ_y was applied to the sinogram from cs_{att} data. Adaptive sinogram filtering was accomplished using these sinograms. Since the sinogram generated from cs_{att} had less noise compared with that from c_{att}, streak artifacts were further reduced, while the z-directional resolution decreased, depending on σ_z and the weighting in the adaptive filter.

2.7. Phantom and data acquisition

An elliptic cylindrical water phantom was used to simulate the abdomen of an adult. The phantom had outer dimensions of 360 mm (width, x-direction) × 210 mm (height, y-direction) × 200 mm (depth, z-direction). To assess the effect of SAR on spatial resolution, a rod object made of acrylic was placed in the water phantom at its center or 100 mm away from its center (Fig. 3a and b). This 100-mm offset position was selected because streak artifacts were conspicuous around this location in the phantom image. The rod had a diameter of 40 mm and a height of 90 mm. The phantom alignment of the rod was adjusted so that the rod axis was completely parallel to the rotation axis of the CT system. The attenuation of the acrylic rod was approximately 130 Hounsfield units (HU) at 120 kV. Consecutive disk images of the acrylic rod were used to measure the spatial resolution using the circular edge method employed in various studies for evaluating performances of IRs [19–22]. To visually evaluate the spatial resolution, a small assembly of three identical acrylic comb-shaped objects (bar-pattern phantom) was placed at the center and 100-mm offset from the center. These comb-shaped objects were arranged horizontally, vertically, and at 45° to represent three orientations as shown in Fig. 3c and d. Each bar (tooth of the comb) was 2 mm wide (a square-wave frequency of 0.25 mm^{-1}) and 5 mm thick. The water-only section of the phantom was used for image noise (standard deviation: SD) measurements. A 320-row multi-slice CT (MSCT) system called Aquilion One (Canon Medical Systems Corp., Otawara, Japan) was used to scan the phantom. Scans were performed with 120 kVp, 0.5 s per rotation, 0.5 × 80 mm detector configuration, and with a pitch factor of 0.81 in helical mode. The tube current was adjusted to obtain a low CT dose index (CTDI) of 5 mGy, which was nearly one third of a standard dose for abdominal CT reported in the diagnostic reference levels in Japan [23]. The CT images were reconstructed with a DFOV of 400 mm, a slice thicknesses of 1.0 mm, and a table increment of 1.0 mm. A reconstruction kernel of FC03 for filtered back projection (FBP) was used.

2.8. In-plane spatial resolution measurement

Disk images from the rod object were analyzed to measure the in-plane modulation transfer functions (MTFs). Prior to the analysis, image averaging was performed using 130 images, which had been obtained by scanning the phantom twice, to improve the contrast-to-noise ratio (CNR) of the averaged image to be analyzed [20–22,24]. CNRs of more than 24 were achieved by this averaging, satisfying the recommendation (CNR>15) in a guideline for CT performance evaluation [25]. Descriptions of the detailed procedures of the circular edge method [19–22] are omitted in this paper. We measured MTFs of the original image and the images processed by SAR with different parameter combinations. In addition, we measured the MTF of the image processed without an adaptive filter to evaluate the effects of the numerical forward projection and subsequent filtered back projection on the spatial resolution. The spatial frequencies at 50%MTF were obtained from the MTF results.

2.9. z-directional spatial resolution

The z-directional spatial resolution was measured from the plane edge at the interface between the rod object used for the in-plane MTF measurement and the water [20,21,26]. For this measurement, we ensured in advance that the rod's plane edge was sufficiently flat and precisely perpendicular to the rod's axis. This measurement was performed only for 3D-SAR with the σ_z parameter. To precisely detect the change in z-directional CT number at the plane edge, 50 consecutive CT images were reconstructed with increments of 0.2 mm. Because of this fine increment, the σ_z parameter was adjusted (increased) by a factor of 5.0 (1.0/0.2) to reproduce the effect of the σ_z parameter applied to image stacks with the normal (1.0-mm) increment. The z-directional edge spread function (ESF) measured from the images including the plane edge was differentiated to yield a line spread function (LSF), which is equal to the slice sensitivity profile (SSP). The full-width at half maximum (FWHM) of SSP was used for the comparison.

2.10. Noise measurement

On a set of images at the water-only section selected from the phantom images, SDs were measured for the regions of interest (ROIs), with 40 × 40 pixels, located at the center and the 100-mm offset positions. The SD values of 10 consecutive images were averaged to produce the results.

2.11. Investigations using abdominal and chest phantoms

Anthropomorphic abdominal and chest phantoms, PH-5 and N-1 (Kyoto Kagaku, Kyoto, Japan), respectively, were scanned using the Aquilion One and a 64-row MSCT system called HD750 (GE Healthcare, Waukesha, WI). For both the Aquilion One and the HD750, the same scan parameters as those for the elliptic cylindrical water phantom were used except for a pitch factor of 0.98 for the HD750. Thus, the low dose condition at 5 mGy was applied to this investigation. A slice thickness of 1 mm and a reconstruction kernel of Standard were selected for image reconstruction with the HD750. The 3D-SAR images were generated from the FBP images of each CT system.

In this investigation, hybrid-type IR performed on the Aquilion One and the HD750, named AIDR 3D and ASiR, respectively, were compared with 3D-SAR. With AIDR 3D, four settings of noise reduction strength are available: Weak, Mild, Standard, and Strong. Mild was selected among them because it was the preferred setting in the hospital participating in this research. The noise reduction strength of ASiR is adjusted by setting the blending ratio between ASiR and FBP (100%: strongest, no blending with FBP). The 100% strength (no blending) was selected to evaluate the performance of ASiR itself. According to a white paper on AIDR 3D, this process reduces noise in projection data using a quantum statistical model and a scanner model; thus, streak artifacts caused by low photon counts are presumed to be suppressed in the reconstructed CT images. In addition to the process in the projection space, AIDR also performs noise reduction in the image space [27]. ASiR reduces image noise using processing that works mainly in the image space [8].

2.12. Artifact index

The artifact reduction capability was evaluated for the phantom images using the following artifact index (AI) estimation method. For each ROI of 15 × 15 pixels in CT image, two sets of SD values were used: SD_P corresponding to those having streak artifacts (p meaning 'presence') and SD_A corresponding to those without streak artifacts ($_A$ meaning 'absence'). For the chest phantom, the SD_P values were measured in areas between the clavicle and the humeral head in five slices at the lung apex level. A representative value of SD_A (SD'_A) was determined by averaging SD_A values in areas just above the scapula in

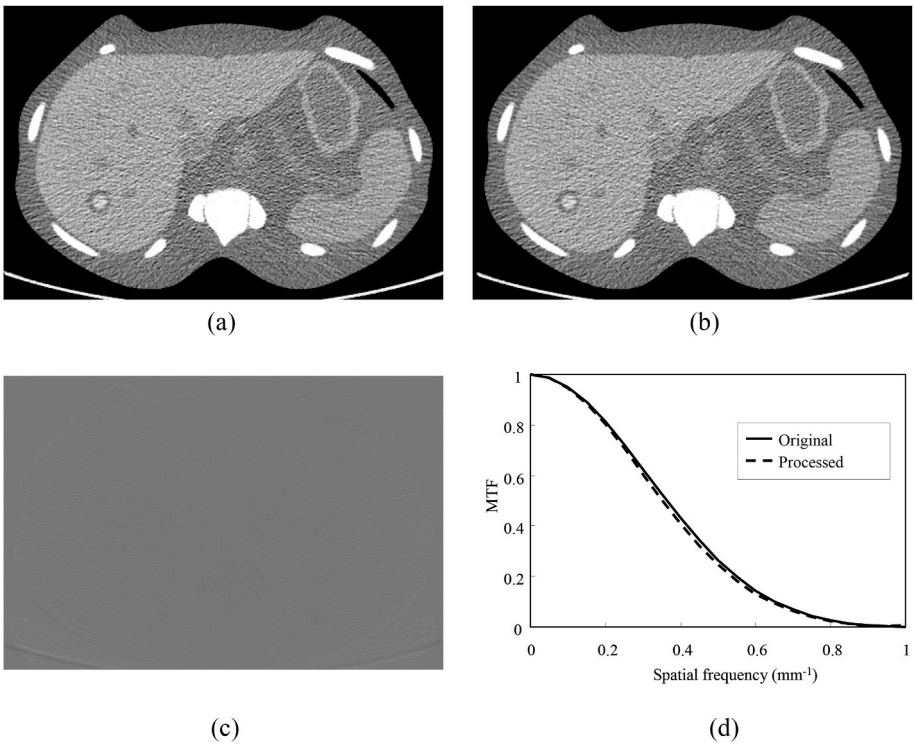

Fig. 4. (a) Original image of an anthropomorphic abdominal phantom, (b) the corresponding image processed with numerical forward projection followed by filtered back projection (without an adaptive filter for streak artifact reduction), and (c) the difference image between them. MTFs corresponding to the original and the processed images are also presented in (d). All the window widths/levels were set at 400/40.

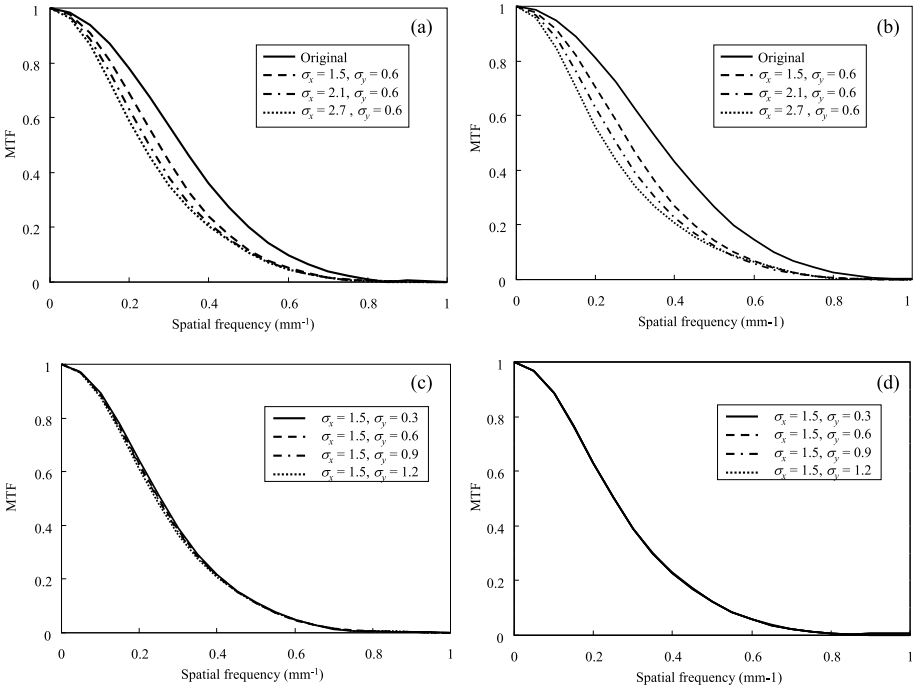

Fig. 5. MTF results of different combinations of σ_x and σ_y for 2D-processing of SAR (2D-SAR) at the 100-mm offset position (a, c) and the center position (b, d).

five slices at the tracheal bifurcation level. For the abdominal phantom, the SD_P values were measured in the liver parenchyma in five slices, which exhibited conspicuous streak artifacts. The SD'_A was determined from areas on the ventral side in five slices at the kidney level. Since the SD'_A values (i.e., original image noise) were significantly different between the image sets compared due to inherent noise difference, we used the normalized AI (nAI) calculated by the following formula:

$$nAI = \sqrt{SD_P{}^2 - SD'_A{}^2} \Big/ SD'_A \tag{6}$$

to cancel out the noise difference [28]. When the nAI value of processed images was not significantly different from that for the original FBP

Table 1
50%MTF results of the original and different combinations of σ_x and σ_y for 2D-SAR. The values in parentheses are the percent decreases from the original.

σ_x	σ_y	50%MTF (mm^{-1})	
		100-mm offset	Center
Original		0.33	0.36
1.5	0.6	0.27 (18%)	0.28 (22%)
2.1	0.6	0.25 (24%)	0.26 (28%)
2.7	0.6	0.23 (30%)	0.23 (36%)
1.5	0.3	0.25 (24%)	0.26 (28%)
1.5	0.9	0.25 (24%)	0.26 (28%)
1.5	1.2	0.24 (27%)	0.26 (28%)

images even though the artifacts appear to be reduced, this indicates that the process simply smoothed the streak artifacts, instead of actually reducing the streak artifacts.

3. Results

3.1. Difference image and MTF

Fig. 4 shows the original image of the abdominal phantom, the corresponding image processed with numerical forward projection followed by filtered back projection (without an adaptive filter), and the difference image between them. The MTF deterioration by the process was slight as shown in Fig. 4d. Weak signals of up to 12 HU were identifiable in the difference images, at high contrast edges between the air and the soft-tissue and between the cortical bone and the soft-tissue.

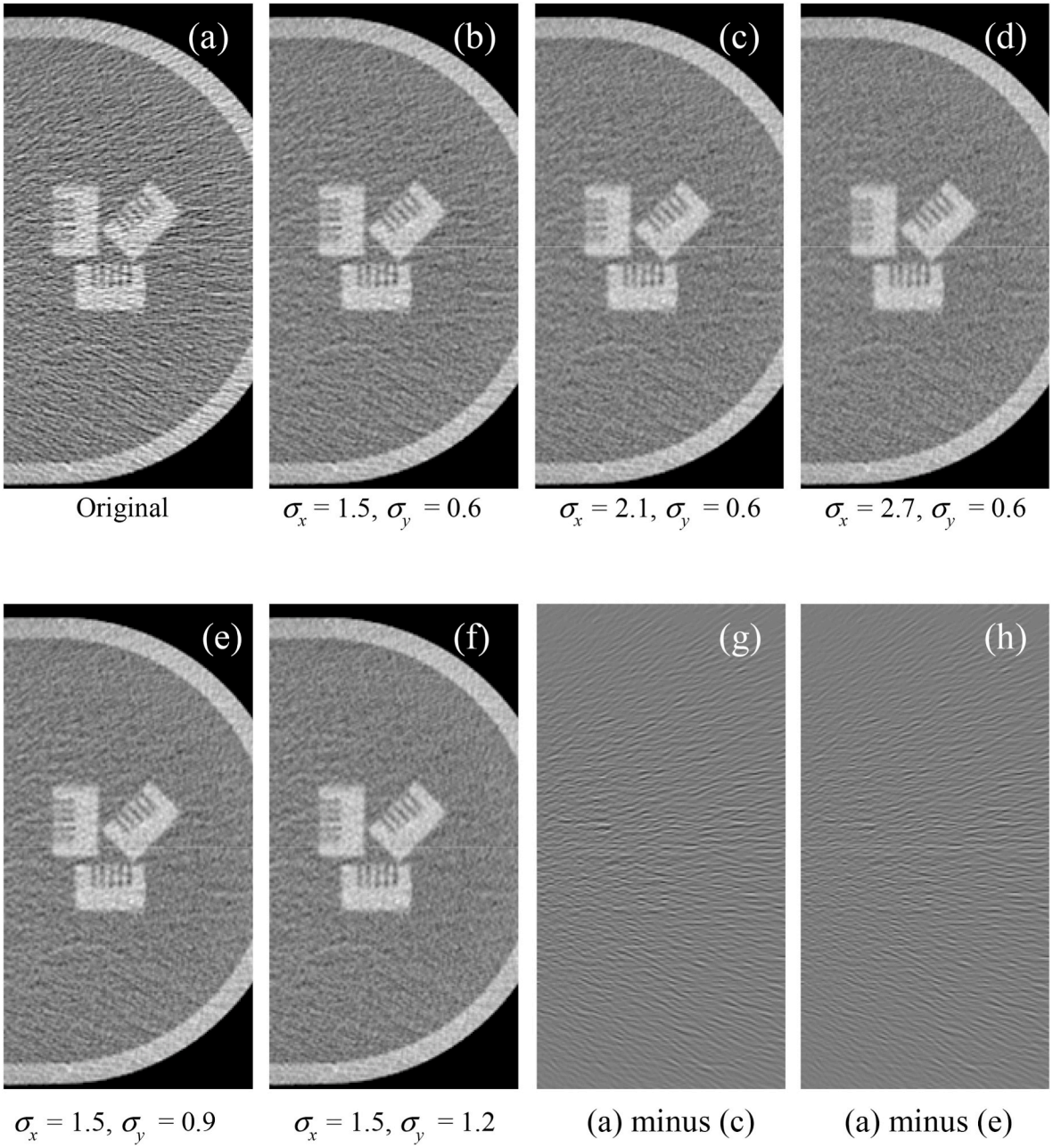

Fig. 6. (a-f) Bar-pattern phantom images of the original and 2D-SAR at the 100-mm offset position. From (b)–(d), the effects of σ_x with σ_y fixed at 0.6 can be observed. From (b), (e), and (f), the effects of σ_y with σ_x fixed at 1.5 can be observed. The difference images between (a) and (c) and between (a) and (e) are also presented in (g) and (h), respectively.

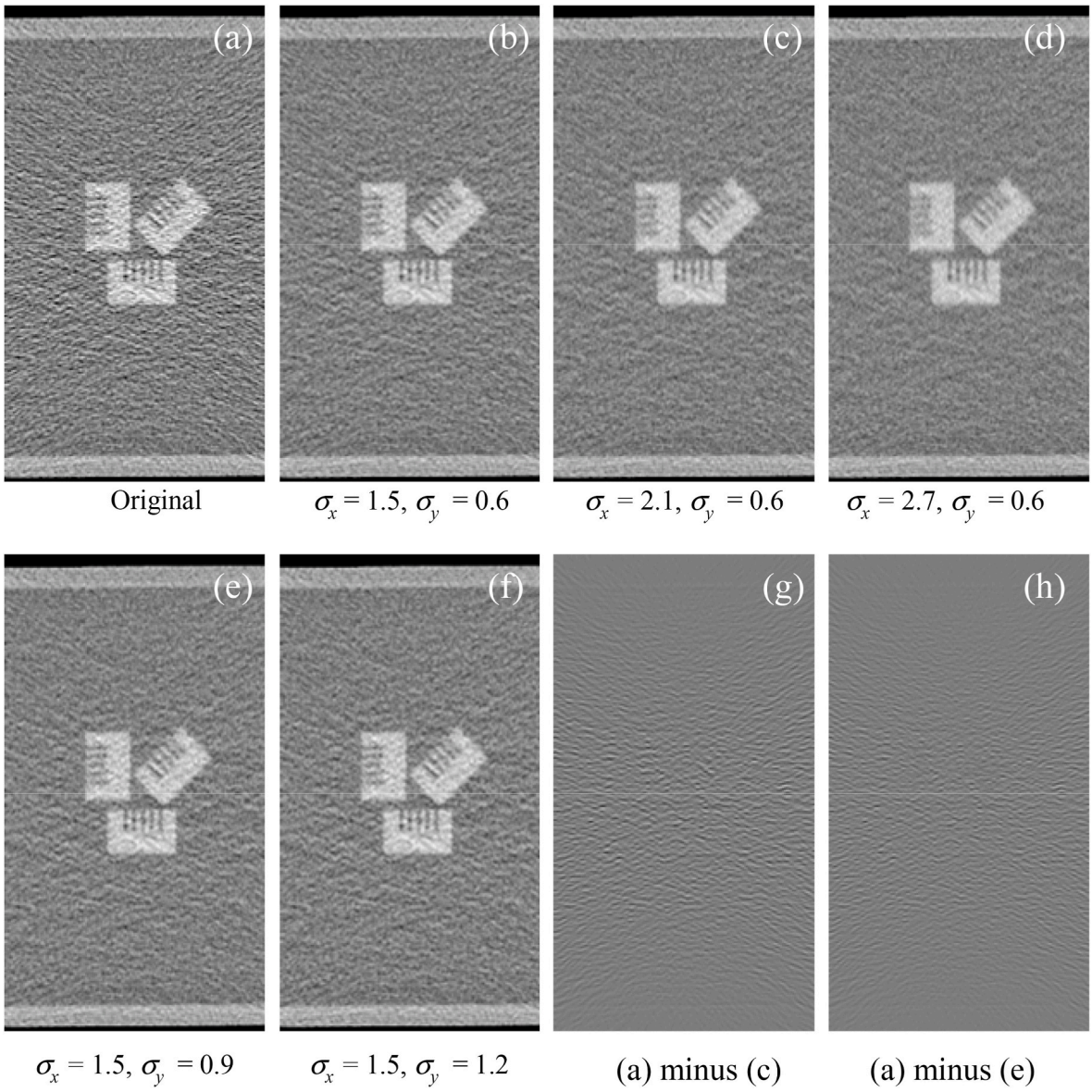

Fig. 7. (a-f) Bar-pattern phantom images of the original and 2D-SAR at the center position. From (b)–(d), the effects of σ_x with σ_y fixed at 0.6 can be observed. From (b), (e), and (f), the effects of σ_y with σ_x fixed at 1.5 can be observed. The difference images between (a) and (c) and between (a) and (e) are also presented in (g) and (h), respectively. All the window widths/levels were set at 400/40.

3.2. *In-plane and z-directional spatial resolution*

Fig. 5 shows MTF results for different combinations of σ_x and σ_y for 2D-SAR. Table 1 summarizes 50%MTF values. With σ_y fixed at 0.6, the MTF decreased with increasing σ_x (Fig. 5a and b), while the percentage decreases of 50%MTF were 18–30% for the offset position and 22–36% for the center position. In contrast, varying the σ_y parameter between 0.3 and 1.2 did not affect MTF at either the offset or the center position (Fig. 5c and d). The measured FWHM (slice thickness) values were 1.14, 1.29, 1.41, and 1.52 mm for the original, $\sigma_z = 0.3$, $\sigma_z = 0.6$, and $\sigma_z = 0.9$, respectively. Fig. 6 presents the original bar-pattern phantom image, the images processed by 2D-SAR, and the difference images between the original and processed images, at the offset position. Considerable streak artifacts were noticeable in the original image due to the low dose of 5 mGy. These artifacts were sufficiently suppressed in the images with the parameter combinations of $\sigma_x = 2.7$ and $\sigma_y = 0.6$; $\sigma_x = 1.5$ and $\sigma_y = 1.2$. However, for the combination of $\sigma_x = 2.7$ and $\sigma_y = 0.6$, a non-negligible deterioration was observed in spatial resolution, corresponding to the 30% decrease in 50%MTF. In the difference image, no signals from the bar-pattern phantom were observed. Fig. 7 shows the phantom images at the center position. The MTF deterioration by $\sigma_x = 2.7$ and $\sigma_y = 0.6$ was more obvious than at the offset position. In addition, the artifacts were almost constant regardless of σ_y, with σ_x fixed at 1.5 (Fig. 7c and d). Slight bar-pattern edge signals were observed in the difference image for the combination of $\sigma_x = 2.1$ and $\sigma_y = 0.6$. Fig. 8 presents axial, coronal, and sagittal phantom images, comparing the original and 3D-SAR ($\sigma_z = 0.3$ to 0.9 with a fixed combination of $\sigma_x = 1.5$ and $\sigma_y = 0.9$), and the difference images for $\sigma_z = 0.6$, at the 100-mm offset position. The streak artifact was notably decreased by the σ_z values of 0.6 and 0.9. However, the σ_z value of 0.9 caused an unfavorable z-directional blurring. The sagittal difference image contains slight signals from the rod edges.

3.3. *Image noise*

Table 2 shows the results of the image noise (SD). The percent noise reduction ranged from 45% to 65% with 2D-SAR and from 48% to 64% with 3D-SAR. The parameter combination of $\sigma_x = 1.5$ and $\sigma_y = 0.9$ for

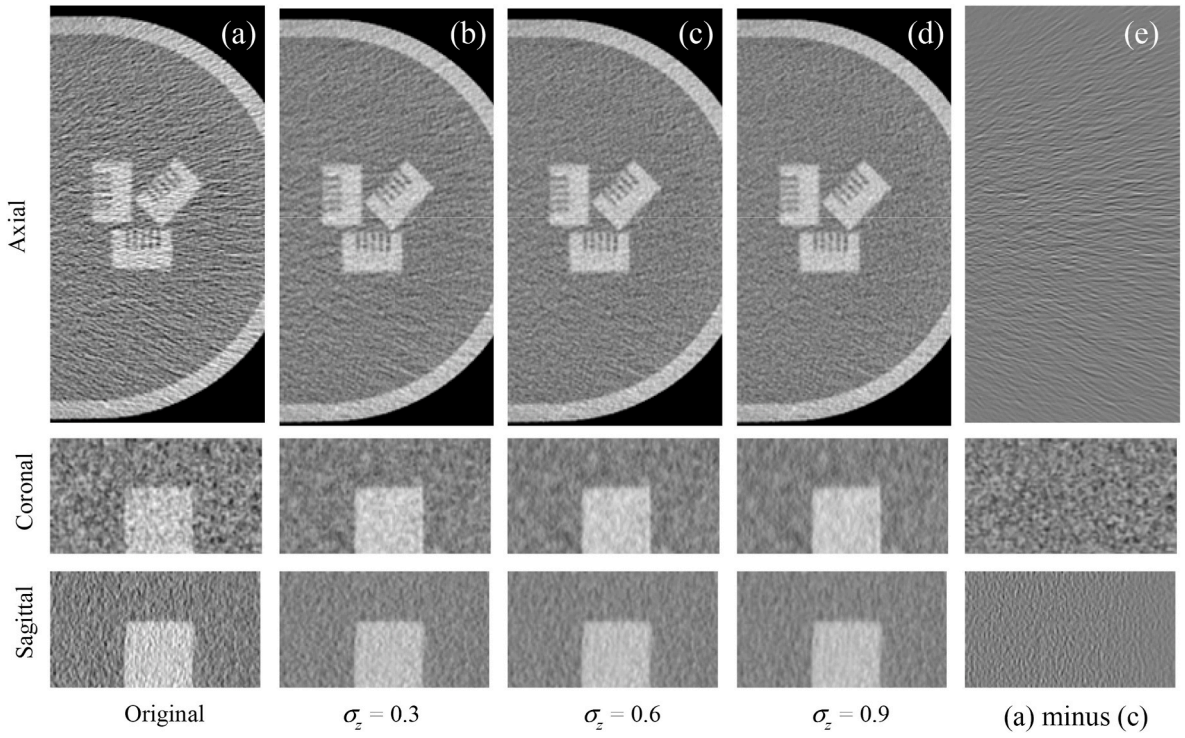

Fig. 8. Axial, coronal, and sagittal bar-pattern phantom images at the 100-mm offset position, comparing the original and 3D-SAR for different values of σ_z, with a fixed combination of $\sigma_x = 1.5$ and $\sigma_y = 0.9$. Difference images between (a) and (c) are also presented in (e). All the window widths/levels were set at 400/40.

Table 2
Results of image noise for the original and different combinations of σ_x and σ_y with 2D-SAR and for the combinations of σ_x, σ_y and σ_z with 3D-SAR. The values in parentheses are the percent decreases from the original.

σ_x	σ_y	σ_z	Standard deviation (HU)	
			100-mm offset	Center
Original			60.6	54.7
1.5	0.6		29.0 (52%)	29.7 (46%)
2.1	0.6		23.8 (61%)	23.8 (56%)
2.7	0.6		20.9 (65%)	20.3 (63%)
1.5	0.3		29.6 (51%)	29.8 (45%)
1.5	0.9		27.3 (54%)	29.6 (46%)
1.5	1.2		25.4 (58%)	29.5 (46%)
1.5	0.6	0.3	27.1 (55%)	28.2 (48%)
1.5	0.6	0.6	23.5 (61%)	23.5 (57%)
1.5	0.6	0.9	21.9 (64%)	21.4 (61%)

2D-SAR, which reduced the bar-pattern visibility only negligibly, gave 54% and 46% noise reductions at the offset and the center positions, respectively. More notable noise reductions (61% and 57% at the offset and the center positions, respectively) were achieved with the parameter combination of $\sigma_x = 1.5$, $\sigma_y = 0.9$, and $\sigma_z = 0.6$ for 3D-SAR.

3.4. Images of abdominal and chest phantoms

Fig. 9 presents the axial and coronal images (obtained by the Aquilion One) of the original, 3D-SAR, and AIDR 3D, and the difference images between the original and 3D-SAR, for the abdominal phantom. A parameter combination of $\sigma_x = 1.5$, $\sigma_y = 0.9$, and $\sigma_z = 0.6$ was used for 3D-SAR. Fig. 10 presents the corresponding images obtained by the HD750. The artifact reduction effect was more evident with the coronal image than with the axial image. In the difference images, although some weak signals from bone edges and boundaries between the air and the soft-tissue were present, no signals from soft-tissue organs were detected. Fig. 11 compares the original, 3D-SAR, and AIDR 3D, and the difference images between the original and 3D-SAR obtained by the Aquilion One, for the chest phantom. Fig. 12 presents the corresponding images obtained by the HD750. We found that 3D-SAR performs artifact reduction as well as AIDR 3D for both the chest and abdomen phantoms. In addition, looking at the bone edges and boundaries of the simulated tumors, we found only a small difference in spatial resolution between the original and 3D-SAR images. The artifact reduction by ASiR of the HD750 was insufficient. Although the artifact appeared to be reduced, streaks, smoothed by noise reduction process in the image space of ASiR, remained. The 3D-SAR effectively reduced streak artifacts of the HD750, as was similarly the case with the Aquilion One.

3.5. Artifact index

Table 3 shows results of nAI. The values of AIDR and 3D-SAR were comparable and notably lower than those of FBP. On the other hand, ASiR did not improve nAI and was notably inferior to 3D-SAR. These were consistent with the artifact reduction observed in the phantom images.

4. Discussion

We have demonstrated, using images of bar-pattern phantoms and anthropomorphic phantoms, that SAR can significantly reduce streak artifacts even though we used, in our analysis, the projection data generated through image-based forward projection instead of real raw-data. The streak artifacts appear along X-ray transmission passes with high attenuations; thus, they generate noise in high-level regions in the projection data (i.e., strong attenuations) generated by the image-based forward projection. This situation is similar to that with real raw-data. Thus, the streak artifacts were reduced by the filtering adaptively applied according to the data level. Though the projection data was generated using the parallel projection, which was different from the fan beam projection based on the real one, the relationship between attenuations and noise levels appeared to be properly reproduced in the

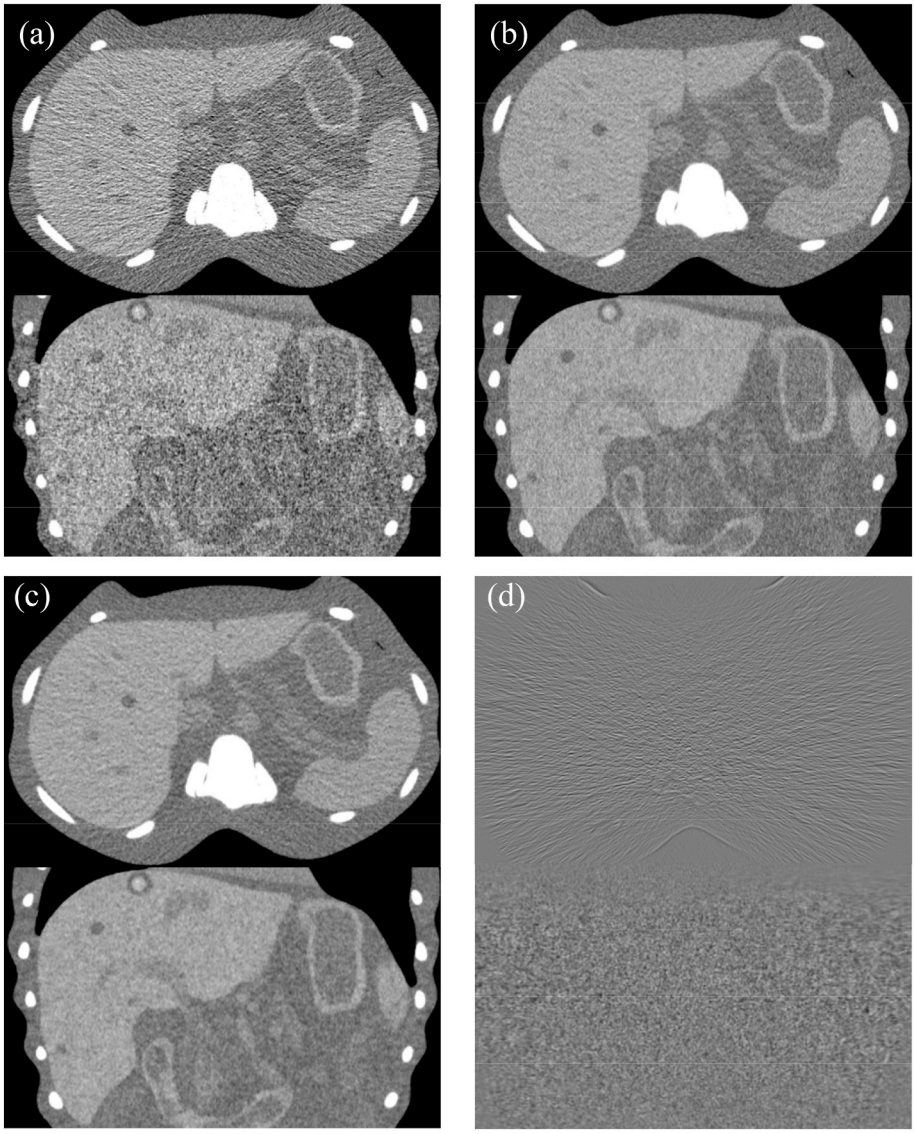

Fig. 9. Axial and coronal image examples of the abdominal phantom, using the Aquilion One: (a) the original; (b) 3D-SAR with $\sigma_x = 1.5$, $\sigma_y = 0.9$, and $\sigma_z = 0.6$; (c) hybrid iterative reconstruction (IR), AIDR 3D; (d) the difference image between (a) and (b). All the window widths/levels were set at 400/40.

projection data, which contributed to the artifact reduction.

When σ_x was large, the in-plane spatial resolution was more affected, and the degree of this effect was more notable at the center position than at offset positions. In contrast, σ_y did not affect the in-plane spatial resolution in most cases. These effects were similarly observed in a previous study that proposed an adaptive filter method using real raw data [4], where the filter parameters in the detector channel and the view angle directions correspond to σ_x and σ_y in our study, respectively. Thus, the degradation in spatial resolution seemed to be unavoidable and should be considered as a cost of the processing that can reduce the streak artifacts.

The 3D processing was found to be more effective in reducing artifacts than 2D-SAR. The influence of the increased slice thickness appeared slight in the phantom images up to $\sigma_z = 0.6$ with a 13% increase of FWHM. In the coronal images of 3D-SAR with this parameter, it was difficult to find a deterioration in z-directional spatial resolution by 3D-processing.

The comparisons of anthropomorphic phantom images between 3D-SAR and AIDR 3D have demonstrated that our proposed technique can deliver sufficient performance in reducing streak artifacts. The nAI values were consistently comparable with the observed artifact reductions (AIDR 3D vs. 3D-SAR: 0.44 vs. 0.30 for the abdominal phantom, 1.07 vs. 0.98 for the chest phantom). Basically, one cannot argue that techniques based on raw data, such as the one implemented in AIDR 3D, are inferior to our technique. The noise in the real projection data was more effectively suppressed by direct noise filtering using projection data in AIDR 3D than by indirect noise reduction using virtual projection data in SAR. Therefore, we believe that SAR's comparable performance in artifact reduction was due to the moderate settings for artifact reduction in AIDR 3D.

In contrast to the results using AIDR 3D, ASiR did not sufficiently reduce streak artifacts because it performs noise reduction mainly in the image space as mentioned earlier. The residual streak artifacts degraded visibilities of the simulated tumors and vessels in the abdominal phantom, whereas the degradations were smaller compared with FBP. The nAI values were comparable between FBP and ASiR (FBP vs. ASiR: 1.85 vs. 1.92 for the abdominal phantom, 2.42 vs. 2.25 for the chest phantom), as was the case with the observed artifacts. Thus, the noise reduction process in ASiR seemed to smooth areas equally regardless of the presence or absence of streak artifacts but to have no sufficient ability to reduce streak artifacts as done by the raw-data-based processing.

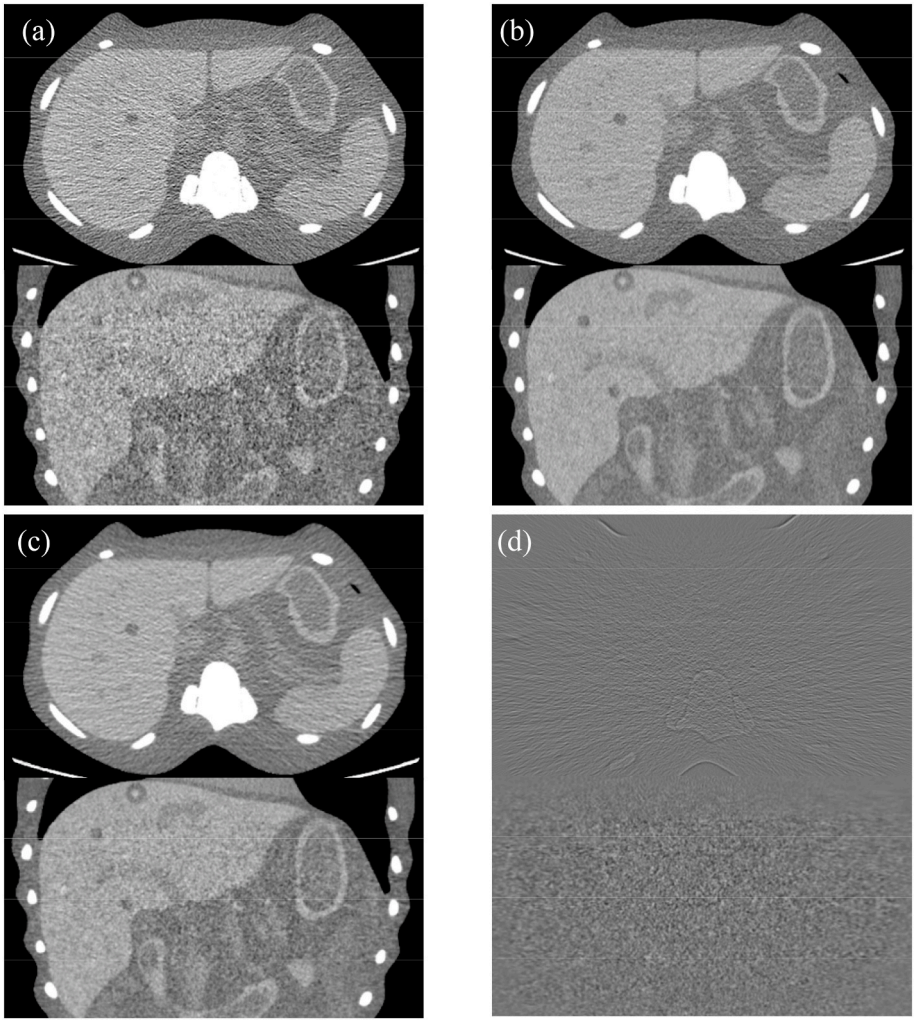

Fig. 10. Axial and coronal image examples of the abdominal phantom, using the HD750: (a) the original; (b) 3D-SAR with $\sigma_x = 1.5$, $\sigma_y = 0.9$, and $\sigma_z = 0.6$; (c) hybrid iterative reconstruction (IR), ASiR; (d) the difference image between (a) and (b). All the window widths/levels were set at 400/40.

We found the filtering of projection data to have some positive effects on the reduction of streak artifacts in certain directions of the image. When projection data (a horizontal profile in the sinogram) was filtered, its effect was basically limited in the direction perpendicular to the projection angle. Owing to this nature, streaks in the limited direction were suppressed (smoothed) without spatial resolution losses in the other directions. Furthermore, the weighting factors in the sinogram were reduced at areas with low attenuations. Thus, most of the object's edges tended to be reproduced by the sinogram data with weak or no filtering. This effect can not be obtained image-based noise reduction techniques because directions, strengths, and locations of the streak artifact are difficult to be correctly identified without using the attenuation data. In other words, some image-based processing for the streak artifact reduction may become possible with help of the attention data obtained through the forward projections.

While this study demonstrated the usefulness of the projection data generated through image-based forward projection in reducing streak artifacts, the outcome indicates some possibility of other uses such as metal artifact reduction. If the metal artifact is not so severe as to make the shape and attenuation of the metal noticeable, the artifact might be reduced through estimations of beam hardening caused by the metal and subsequent projection data correction based on the estimations.

Admittedly, this study has a few limitations. First, SAR cannot be reliably applied to enlarged CT images reconstructed with a DFOV smaller than the full width of the body contour (usually the width of a transverse section of the body). This is a shortcoming inherent in SAR in that its application is rather limited. Whereas the chest phantom we used had a simulated bone structure, the abdominal phantom had some simulated soft-tissue organs and tumors in addition to a simulated bone structure. However, various fat components and soft-tissue organs were missing in both of them. Thus, while x-ray attenuations were fairly closely simulated with these phantoms, not all kinds of artifact were reproduced. Finally, we did not particularly investigate ways to optimize parameter settings because we regarded this study just as a pilot study to quickly examine the feasibility of SAR. As mentioned earlier, TCM is commonly used today; thus, the noise level tends to be nearly constant for practically all body sizes, and so does the streak artifact. Since SAR is image-based, it should be straightforward to adjust the processing parameters for each run of SAR. Thus, the effects of adjusting parameters σ_x and σ_z can be easily observed, facilitating the determination of the parameters.

5. Conclusion

This study has proposed a streak artifact reduction (SAR) technique that consists of three steps: numerical forward projection to a CT image, adaptive filtering of the generated sinogram, and image reconstruction from the processed sinogram. This technique sufficiently reduced the streak artifacts caused by low photon counts without accessing the raw data. While SAR degraded the spatial resolution measured by MTF to

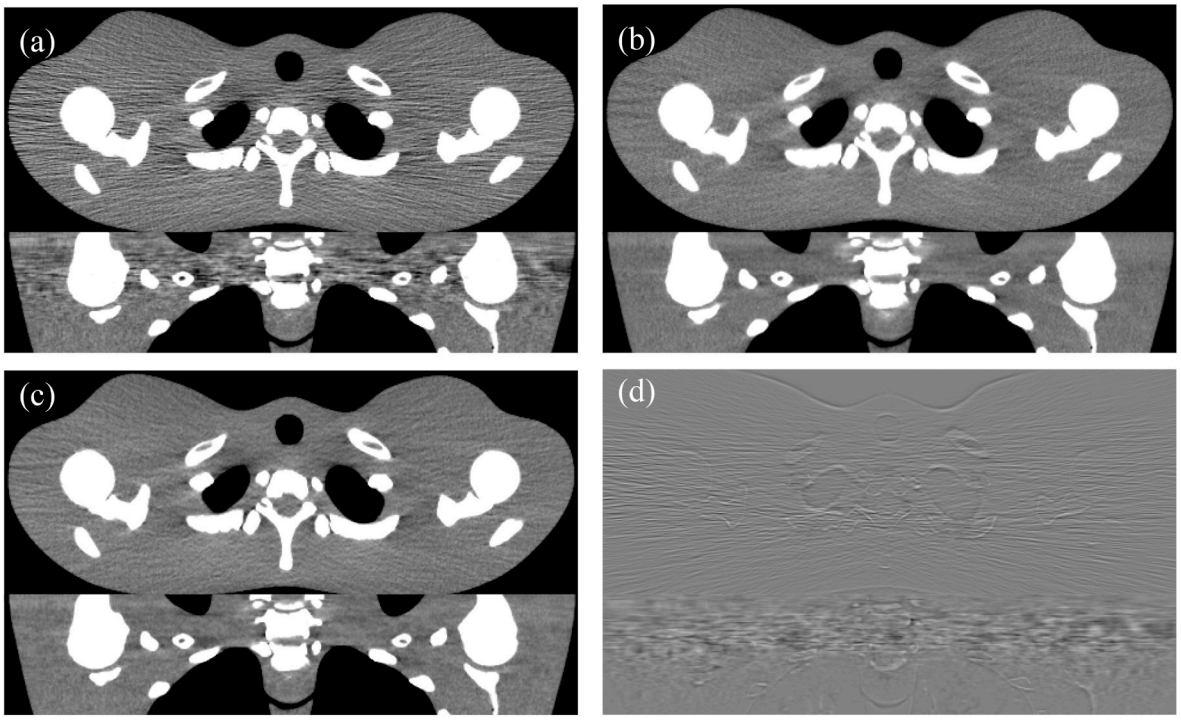

Fig. 11. Axial and coronal image examples of the chest phantom, using the Aquilion One: (a) the original; (b) 3D-SAR with $\sigma_x = 1.5$, $\sigma_y = 0.9$, and $\sigma_z = 0.6$; (c) AIDR 3D; (d) the difference image between (a) and (b). All the window widths/levels were set at 400/40.

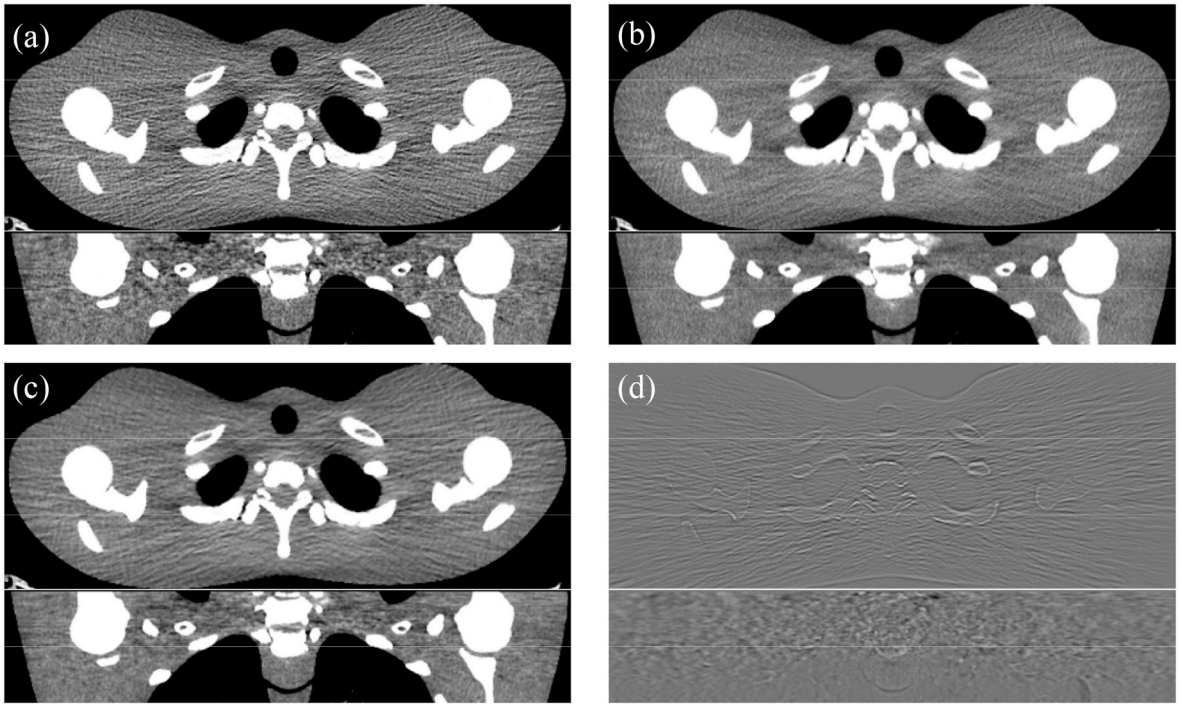

Fig. 12. Axial and coronal image examples of the chest phantom, using the HD750: (a) the original; (b) 3D-SAR with $\sigma_x = 1.5$, $\sigma_y = 0.9$, and $\sigma_z = 0.6$; (c) ASiR; (d) the difference image between (a) and (b). All the window widths/levels were set at 400/40.

some degree, the effects were limited in the abdominal and chest phantom images. A 3D version of SAR using consecutive CT images has further enhanced the effectiveness, offering artifact reduction performance comparable to that of the hybrid type IR (AIDR 3D), which used a raw-data-based process as well, and notably better than that of the hybrid type IR (ASiR), which used only image-based processing.

Since it does not require raw data, SAR will be a promising tool for improving CT image quality, applicable to most CT images generated by various systems from different vendors.

Table 3
Results of artifact index (nAI) measured from the abdominal and chest phantom images.

	Abdominal phantom	Chest phantom
	Aquilion One	
FBP	1.55 ± 0.12	3.81 ± 0.17
AIDR 3D	0.44 ± 0.06	1.07 ± 0.07
3D-SAR	0.30 ± 0.05	0.98 ± 0.06
	HD750	
FBP	1.85 ± 0.10	2.42 ± 0.16
ASiR	1.92 ± 0.11	2.25 ± 0.14
3D-SAR	0.39 ± 0.04	0.51 ± 0.06

Funding

This research did not receive any specific grant from funding agencies in the public, commercial, or not-for-profit sectors.

Declaration of competing interest

None declared.

References

[1] J.F. Barrett, N. Keat, Artifacts in CT: recognition and avoidance, Radiographics 24 (2004) 1679–1691, https://doi.org/10.1148/rg.246045065.
[2] B. Sahiner, A.E. Yagle, Reconstruction from projections under time-frequency constraints, IEEE Trans. Med. Imag. 14 (2) (1995) 193–204, https://doi.org/10.1109/42.387701.
[3] J. Hsieh, Adaptive streak artifact reduction in computed tomography resulting from excessive x-ray photon noise, Med. Phys. 25 (11) (1998) 2139–2147, https://doi.org/10.1118/1.598410.
[4] M. Kachelriess, O. Watzke, W.A. Kalender, Generalized multi-dimensional adaptive filtering for conventional and spiral single-slice, multi-slice, and cone-beam CT, Med. Phys. 28 (4) (2001) 475–490, https://doi.org/10.1118/1.1358303.
[5] M. Katsura, J. Sato, M. Akahane, I. Matsuda, M. Ishida, K. Yasaka, et al., Comparison of pure and hybrid iterative reconstruction techniques with conventional filtered back projection: image quality assessment in the cervicothoracic region, Eur. J. Radiol. 82 (2) (2013) 356–360.
[6] E.W. Olcott, L.K. Shin, G. Sommer, I. Chan, J. Rosenberg, F.L. Molvin, et al., Model-based iterative reconstruction compared to adaptive statistical iterative reconstruction and filtered back-projection in CT of the kidneys and the adjacent retroperitoneum, Acad. Radiol. 21 (6) (2014) 774–784.
[7] Y. Jia, B. Zhai, T. He, Y. Yu, N. Yu, H. Duan, et al., The application of a new model-based iterative reconstruction in low-dose upper abdominal CT, Acad. Radiol. 26 (10) (2019) e275–e283.
[8] E.C. Ehman, L. Yu, A. Manduca, A.K. Hara, M.M. Shiung, D. Jondal, et al., Methods for clinical evaluation of noise reduction techniques in abdominopelvic CT, Radiographics 34 (4) (2014) 849–862.
[9] J. JHsieh, E. Liu, B. Nett, J. Tang, J.B. Thibault, S. Sahney, A new era of image reconstruction: TrueFidelity™. Technical white paper on deep learning image reconstruction, GE Healthcare (2019).
[10] R. Singh, S.R. Digumarthy, V.V. Muse, A.R. Kambadakone, M.A. Blake, A. Tabari, et al., Image quality and lesion detection on deep learning reconstruction and iterative reconstruction of submillisievert chest and abdominal CT, AJR Am. J. Roentgenol. 214 (3) (2020) 566–573.
[11] J.H. Kim, H.J. Yoon, E. Lee, I. Kim, Y.K. Cha, S.H. Bak, Validation of deep-learning image reconstruction for low-dose chest computed tomography scan: emphasis on image quality and noise, Korean J. Radiol. 22 (1) (2021) 131–138.
[12] L.L. Geyer, U.J. Schoepf, F.G. Meinel, J.W. Nance, G. Bastarrika, J.A. Leipsic, et al., State of the art: iterative CT reconstruction techniques, Radiology 276 (2) (2015) 339–357.
[13] Y. Nishiyama, K. Tada, H. Mori, M. Maruyama, T. Katsube, N. Yamamoto, et al., Effect of the forward-projected model-based iterative reconstruction solution algorithm on image quality and radiation dose in pediatric cardiac computed tomography, Pediatr. Radiol. 46 (12) (2016) 1663–1670.
[14] M. Beister, D. Kolditz, W.A. Kalender, Iterative reconstruction methods in X-ray CT, Phys. Med. 28 (2) (2012) 94–108.
[15] B. Chen, S. Leng, L. Yu, Z. Yu, C. Ma, C. McCollough, Lesion insertion in the projection domain: methods and initial results, Med. Phys. 42 (12) (2015) 7034–7042.
[16] Y. Zhang, H. Yu, Convolutional neural network based metal artifact reduction in X-ray computed tomography, IEEE Trans. Med. Imag. 37 (6) (2018) 1370–1381.
[17] E.V.R. Di Bella, A.B. Barclay, R.L. Eisner, R.W. Schafer, A comparison of rotation-based methods for iterative reconstruction algorithms, IEEE Trans. Nucl. Sci. 43 (6) (1996) 3370–3376, https://doi.org/10.1109/23.552756.
[18] S.K. Park, R.A. Schowengerdt, Image reconstruction by parametric cubic convolution, Comput. Vis. Graph Image Process 23 (1983) 258–272, https://doi.org/10.1016/0734-189X(83)90026-9.
[19] S. Richard, D.B. Husarik, G. Yadava, S.N. Murphy, E. Samei, Towards task-based assessment of CT performance: system and object MTF across different reconstruction algorithms, Med. Phys. 39 (7) (2012) 4115–4122, https://doi.org/10.1118/1.4725171.
[20] H. Kawashima, K. Ichikawa, K. Matsubara, H. Nagata, T. Takata, S. Kobayashi, Quality evaluation of image-based iterative reconstruction for CT: comparison with hybrid iterative reconstruction, J. Appl. Clin. Med. Phys. 20 (6) (2019) 199–205, https://doi.org/10.1002/acm2.12597.
[21] K. Ichikawa, H. Kawashima, M. Shimada, T. Adachi, T. Takata, A three-dimensional cross-directional bilateral filter for edge-preserving noise reduction of low-dose computed tomography images, Comput. Biol. Med. 111 (2019) 103353, https://doi.org/10.1016/j.compbiomed.2019.103353.
[22] T. Takata, K. Ichikawa, W. Mitsui, H. Hayashi, K. Minehiro, K. Sakuta, et al., Object shape dependency of in-plane resolution for iterative reconstruction of computed tomography, Phys. Med. 33 (2017) 146–151, https://doi.org/10.1016/j.ejmp.2017.01.001.
[23] National diagnostic reference levels in Japan (2020)—Japan, 2020. DRLs, https://www.radher.jp/J-RIME/report/DRL2020_Engver.pdf. (Accessed 10 December 2020).
[24] L. Yu, T.J. Vrieze, S. Leng, J.G. Fletcher, C.H. McCollough, Technical Note: measuring contrast- and noise-dependent spatial resolution of an iterative reconstruction method in CT using ensemble averaging, Med. Phys. 42 (5) (2015) 2261–2267, https://doi.org/10.1118/1.4916802.
[25] E. Samei, D. Bakalyar, K.L. Boedeker, S. Brady, J. Fan, S. Leng, et al., Performance evaluation of computed tomography systems: summary of AAPM Task Group 233, Med. Phys. 46 (11) (2019) e735–e756, https://doi.org/10.1002/mp.13763.
[26] B. Chen, O. Christianson, J.M. Wilson, E. Samei, Assessment of volumetric noise and resolution performance for linear and nonlinear CT reconstruction methods, Med. Phys. 41 (7) (2014), 071909, https://doi.org/10.1118/1.4881519.
[27] Irwan R, Nakanishi S, Blum A, AIDR 3D - Reduces dose and simultaneously improves image quality (White Paper) . Toshiba Med. Syst.. Available from: https://us.medical.canon/download/aidr-3d-wp-aidr-3d (Accessed 10 December 2020).
[28] H. Kawashima, K. Ichikawa, T. Takata, W. Mitsui, Algorithm-based artifact reduction in patients with arms-down positioning in computed tomography, Phys. Med. 69 (2020) 61–69.